

PAPER • OPEN ACCESS

## Two-level bulk microfabrication of a mechanical broadband vibration amplitude-amplifier with ten coupled resonators

To cite this article: Michelle Müller *et al* 2018 *J. Micromech. Microeng.* **28** 045009

View the [article online](#) for updates and enhancements.

You may also like

- [Microfabrication of multi-layer glassy carbon microstructures through dye-doped negative photoresists](#)  
Ryan Burks, Zachariah Walker, Colin O'Neill *et al.*
- [Microfeatures and microfabrication: current role of micro-electric discharge machining](#)  
S K Singh and H S Mali
- [Prototyping of a highly performant and integrated piezoresistive force sensor for microscale applications](#)  
Bilal Komati, Joël Agnus, Cédric Clévy *et al.*

# Two-level bulk microfabrication of a mechanical broadband vibration amplitude-amplifier with ten coupled resonators

Michelle Müller<sup>1</sup> , Verena Maiwald<sup>1</sup>, Lothar Thiele<sup>2</sup>, Jan Beutel<sup>2</sup>,  
Cosmin Roman<sup>1</sup> and Christofer Hierold<sup>1</sup>

<sup>1</sup> Department of Mechanical and Process Engineering, Micro and Nanosystems Group, ETH Zurich, 8092 Zurich, Switzerland

<sup>2</sup> Department of Information Technology and Electrical Engineering, Computer Engineering and Networks Laboratory, ETH Zurich, 8092 Zurich, Switzerland

E-mail: [michelle.mueller@micro.mavt.ethz.ch](mailto:michelle.mueller@micro.mavt.ethz.ch)

Received 14 December 2017

Accepted for publication 31 January 2018


Published 19 February 2018



## Abstract

A micromechanical broadband vibration amplitude-amplifier for low power detection of acoustic emission signals is presented. It is based on a coupled mass-spring system and was fabricated in a two-level bulk microfabrication process. The device consists of ten resonators coupled in series, which decrease in mass by a factor of three each, to achieve a high amplification over a broad bandwidth. The fabrication process for this multiscale device is based on front- and backside etching of a silicon-on-insulator wafer. It enables coupling MEMS resonators of two different thicknesses with a weight ratio from largest to smallest mass of 26'244 and reduces die size by resonator stacking. The first ten eigenmodes of the device are in-plane and unidirectional. Steady-state and transient response of the device in comparison to a 1D lumped element model is presented. An average amplitude amplification of 295 over a bandwidth of 10.7 kHz (4.4–15.1 kHz) is achieved and can be reached in less than 1 ms. Applications are low-power detection of short broadband vibration signals e.g. for structural health monitoring (cliffs, pipelines, bridges).

Keywords: multiscale MEMS, multi-degree of freedom, mechanical vibration amplification, two-level microfabrication, coupled masses, band-pass

 Supplementary material for this article is available [online](#)

(Some figures may appear in colour only in the online journal)

## 1. Introduction

High mechanical vibration amplification over a specific bandwidth is interesting for detecting weak broadband vibrations, such as acoustic emissions in structural health monitoring or microseismic events [1]. Various solutions for mechanical motion amplification have previously been demonstrated.

Compliant mechanisms are used to increase motion amplitudes. In [2], the sensitivity of a MEMS accelerometer was improved by compliant microlevers. Similarly, displacement amplification by a compliant mechanism was demonstrated in [3].

Unlike compliant mechanisms, motion amplifiers based on coupled mass-spring systems are frequency selective. Two degrees of freedom (DOF) micromachined resonators have been demonstrated by mechanically linking two mass-spring-damping units together [4]. A three DOF mechanically coupled bandpass filter was applied for harvesting energy from ambient vibrations [5]. Dual-mass vibration energy harvesters



Original content from this work may be used under the terms of the [Creative Commons Attribution 3.0 licence](#). Any further distribution of this work must maintain attribution to the author(s) and the title of the work, journal citation and DOI.

have been implemented at the macroscale [6, 7], achieving 51 times power amplification [8].

Here, mechanical vibration amplitude-amplification is obtained by coupling multiple resonators in series, while spring stiffnesses and masses decrease towards the end of the chain. Low vibrations at the large outermost mass travel towards the last and smallest mass in the chain with increasing oscillation amplitude. Previously, we have demonstrated an in-plane system with 6 coupled resonators, where the masses increase by a factor of two, with average amplification of 15.8 [9, 10], and an out-of-plane system with 8 coupled resonators and an average amplification of 57.8 [11]. Coupling more resonators and increasing the weight ratio between biggest to smallest mass increases the amplification. However, adding masses becomes technologically very challenging beyond a certain point.

A key challenge in up-scaling the coupled mass-spring amplitude-amplifier concept we introduced earlier [10] is the exponential increase of the masses with the number of degrees of freedom. Conventional planar microfabrication technologies utilize mainly single functional layers, e.g. the device layer of an SOI wafer. Realizing large masses in a single thin layer would consume prohibitively large surface area and is thus not practical. SOI microfabrication processes have been proposed where, additionally to the device layer, the handle layer was utilized to increase the seismic mass of a high sensitivity in-plane accelerometer [12, 13]. Further, multi-level surface microfabrication processes have been presented [14, 15]. However, they are limited to thin layers of few  $\mu\text{m}$ .

As solution, we propose to expand the device over two silicon layers of varying thicknesses. The smaller masses are defined in the thinner layer, while the larger masses are in the thicker or both layers. This two-level architecture can be achieved for example by using the handle and device layer of a silicon-on-insulator (SOI) wafer.

Even with a two-level approach, several challenges remain in the bulk microfabrication of a multiscale device with many degrees of freedom. First, a design has to be developed where undesired eigenmodes (out-of-plane-, rotational- and gimbal-modes) are avoided within the bandwidth of interest, as they may degrade device performance. Second, the multiscale device is susceptible to warping by intrinsic stress, which thus has to be kept at a minimum. Further, matching natural frequencies of the resonators over the two layers has to be achieved.

In this paper, we overcome several major obstacles in the path of upscaling the previously presented proof-of-concept device [10]. The mechanical amplitude-amplifier introduced in [10] has a number of very desirable features, including high-amplification over a wide bandwidth and off-resonant amplification, which allows it to respond very fast. Yet, as outlined above, upscaling presents a number of technical challenges, which are addressed in this paper. Besides that, to our knowledge, we achieve the highest purely mechanical vibration amplitude-amplification (295 average) over a broad bandwidth (10.7 kHz) so far.

The paper is structured as follows: in the second section, the general device concept as well as the design and modeling is introduced. The third section covers methods such as

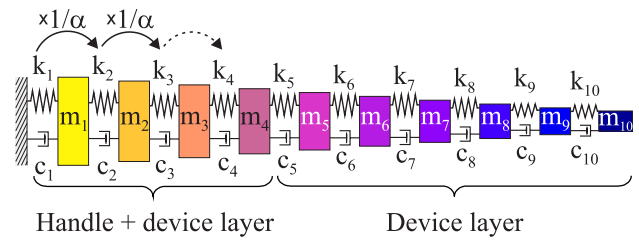


**Figure 1.** Schematic of coupled mass-spring vibration amplifier with ten coupled resonators. The spring stiffnesses decrease by a factor  $\alpha$  from the first resonator, which is anchored to the substrate, towards the last resonator in the chain. The individual resonators have the same eigenfrequency. For the presented amplifier, the resonators are distributed over two Si layers (handle and device layer of an SOI wafer).

fabrication and characterization of the device. Subsequently, fabrication and measurement results, including steady-state and transient response of the device, are presented in section four and discussed in section five. Finally, a conclusion is given in section six.

## 2. Device concept and design

### 2.1. Concept

There are two design rules for the coupled mass-spring amplifier. First, all individual mass-spring pairs have the same eigenfrequency:

$$\omega_0 = 2\pi f_0 = \sqrt{\frac{k_i + k_{i+1}}{m_i}} = \sqrt{\frac{k_n}{m_n}}, i = 1, \dots, n - 1. \quad (1)$$

Secondly, the spring stiffnesses decrease by a factor  $\alpha$ :

$$k_{i+1} = \frac{k_i}{\alpha}, i = 1, \dots, n - 1. \quad (2)$$

The basic design and corresponding rules are schematically portrayed in figure 1. Once frequency  $\omega_0$ , factor  $\alpha$  and the mass or spring stiffness of one resonator are chosen, all other masses and spring stiffnesses are determined by equations (1) and (2). The masses decrease similar to the spring stiffnesses with factor  $\alpha$ , except for the last mass. With these design rules, weak vibrations exciting the first resonator are amplified while traveling towards the last resonator, if they are within the allowed frequency band.

An example of a frequency response of the last resonator is given in figure 2. The amplitude of  $m_{10}$  ( $Y_{10}$ ) is divided by the amplitude of the sensor package ( $Y_0$ ). Corresponding to the ten resonators with each one DOF, ten resonance peaks are visible. The bandwidth is defined from the first to the last observable resonance peak. Average and minimum amplification of displacements are determined within this bandwidth.

The given simple design rules result in a Pareto-like solution for bandwidth and minimum amplification (see supplementary data, section 1 ([stacks.iop.org/JMM/28/045009/mmedia](http://stacks.iop.org/JMM/28/045009/mmedia))). We do not rule out that other designs may yield similar high amplification over a broad bandwidth, but it is not clear to us how those designs could be found besides an exhaustive numerical search.

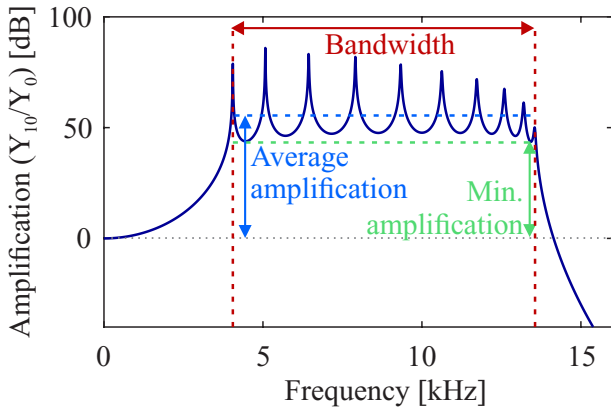


**Figure 2.** Simulated frequency response of  $m_{10}$ . Bandwidth is defined from first to last observable resonant peak. Average and minimum amplitude-amplification are determined within this bandwidth.

Our device has a band-pass response comparable to conventional electromechanical band-pass filters which consist of two identical resonators connected through a coupling spring [16]. It was shown that higher order filters with more coupled resonators achieve a better selectivity [17, 18]. However, natural frequencies of the individual resonators have to be well matched to avoid passband distortion [17]. In contrast to the system presented here, filters are configured to transmit signals in a specific frequency range, with ideal transmittance of one, thus no amplification of the input signal amplitude is achieved.

The amplification in our device is based on coupled decreasing masses. Similar, dual-mass vibration energy harvesters are based on two resonators coupled in series [6–8]. By first coupling an intermediate large mass to the vibrating substrate, followed by the harvester with a smaller mass, a motion amplification can be achieved. Bandwidth and amplification in those system can be tuned by selecting the masses and springs separately [8], but often resonators with identical natural frequencies are chosen [6, 7].

### 2.2. Amplification and bandwidth design

To obtain a specific amplification and bandwidth, the number of coupled resonators  $n$  and the factor  $\alpha$  must be optimized. An overview of possible combinations and resulting bandwidth and minimum amplification is given in figure 3. The design space is limited to the solid lines as the number of resonators  $n$  is confined to natural numbers. Increasing the number of resonators introduces more natural modes and thus broadens the bandwidth and increases the minimum amplification at the same time. A larger factor  $\alpha$  decreases the bandwidth but increases the minimum amplification.

The mechanical amplifier is intended for the detection of short vibration bursts in the very low acoustic emission range of few kHz to observe rock damage [19]. Another application in this frequency range is pipeline monitoring [20]. The eigenfrequency of the individual resonators was chosen as  $f_0 = 12.5$  kHz. It was further decided to couple ten resonators ( $n = 10$ ) where the masses decrease by a factor three ( $\alpha = 3$ ),

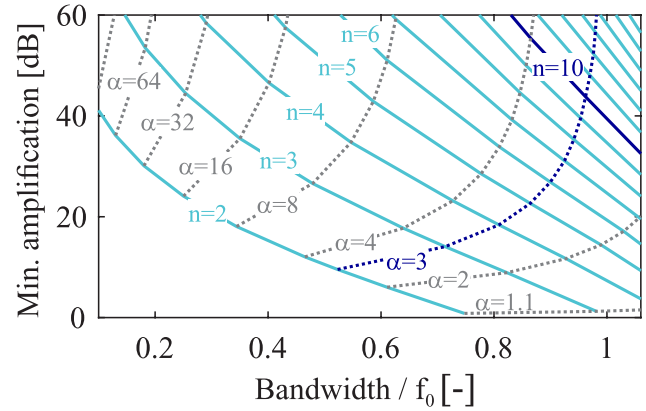


**Figure 3.** Achievable minimum amplification and bandwidth depending on the number of coupled resonators  $n$  and the spring stiffness decreasing factor  $\alpha$ . Design space is limited to the solid lines, as  $n$  is confined to natural numbers. Highlighted are the parameters chosen for the presented device.

which covers a bandwidth of 12 kHz with a minimum amplification of 150 (43.4 dB).

In the proposed two-level design, resonators are distributed over the device and handle layer of an SOI wafer. Six resonators are in the device and four are also in the handle layer (figure 1). The springs are only in the device or the handle layer. This design imposes challenges on the natural frequency matching of the resonators, since device and handle layer springs differ in design and are formed in separate fabrication steps. A good matching must be obtained to achieve an undistorted amplification band [17]. Mainly the higher frequencies in the amplification band are affected if the device and handle layer springs are not well matched (figure 4). For 20% stiffer springs in the device layer compared to the handle layer, all modes but especially the higher ones are shifted to increased frequencies and amplification is lowered. The reverse observation can be made for softer springs.

### 2.3. Structural design

Finite element analysis (FEA) was utilized to find a design which fulfills the design rules (1) and (2). Iteratively, eigenfrequency and achieved spring stiffness with resulting effective mass were simulated for each resonator and the design was accordingly adapted until an optimal form for each resonator was found. Damping was not considered. The design of the resonators was further strongly influenced by the achieved mode shapes of the overall device. It was desired to obtain a device with the first ten eigenmodes corresponding to the classical coupled mass-spring model with 10 DOF, without any gimbal modes as seen in [11]. Design advice is given in [9]. For example, many soft springs distributed around the mass instead of a few stiff ones increase the torsional stiffness. Also, a circular mass shape reduces rotational moments. Further, the inset of springs decreases the bending length of the masses and prohibits out-of-plane modes where the resonators behave similar to a membrane. Along this reasoning, only six masses were placed in the handle layer, as the aspect ratio of a seventh mass would turn it into a membrane rather

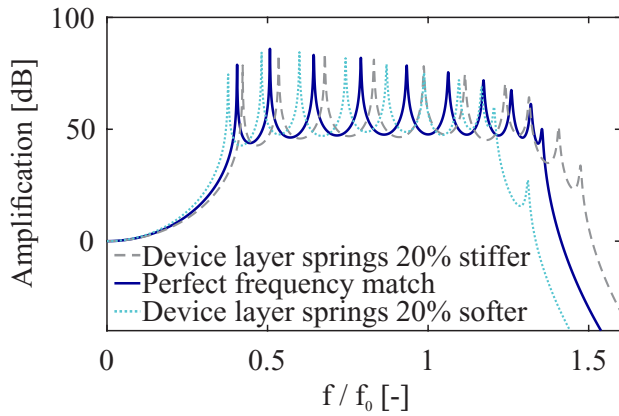


**Figure 4.** Transfer function of  $m_{10}$  obtained with a lumped element model showing the influence of frequency matching between resonators of the two layers. For softer device layer springs compared to handle layer springs, amplification is reduced, whereas for stiffer device layer springs bandwidth is reduced.

than a resonator and its first eigenmode would be out-of-plane. Optimized mass designs in the device layer could be adapted for the handle layer, e.g. mass  $m_1$  is similar in shape to  $m_6$ , as well as  $m_2$  to  $m_7$ .

The chosen parameters result in a mass-ratio of first to last mass of  $m_1/m_{10} = (1 + \alpha)\alpha^{n-2} = 26'244$ . Thus the lower boundary of the device size is determined by the last mass. In our case,  $m_{10}$  is equipped with gap-closing capacitance electrodes with static counterelectrodes and bondpads for electrical connection next to it. This enables capacitive readout of the last mass in future applications.

For a more compact device, resonators in the handle layer can be stacked underneath resonators in the device layer. Handle and device layer are functionally connected at mass  $m_4$  through the buried oxide (BOX) at twelve locations. A schematic cross-section of such a connection is shown in figure 5. The device is two-fold axis symmetric and a top-view of a corner of the device is given in figure 6. A corresponding tilted cross-section reveals the thickness of the layers. The device layer resonators are suspended by a  $2 \mu\text{m}$  gap from the handle layer resonators. A support wafer protects and suspends the handle layer resonators.

### 3. Methods

#### 3.1. Fabrication

The amplifier is fabricated in a two-level bulk microfabrication process. It is based on an SOI wafer, where both Si layers contain parts of the device. Here, a (100)-SOI wafer with  $40 \mu\text{m}$  device,  $2 \mu\text{m}$  BOX and  $500 \mu\text{m}$  handle layer was used. Crystallinity and doping is the same in both layers as well as in the double-side-polished (DSP) support wafer. Materials were limited to single crystalline Si and  $\text{SiO}_2$  to keep the thermal expansion mismatch as low as possible. A relatively thin BOX layer, which was additionally retained on the handle layer side of the SOI wafer, was chosen to obtain a minimal wafer bow [21]. A thick device layer was taken along the same reasoning.

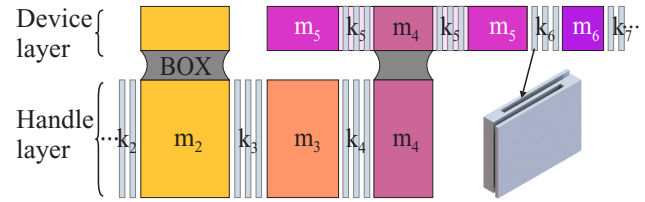


**Figure 5.** Schematic of connection between masses in the device and handle layer (not to scale). Handle and device layer are connected at  $m_4$  through the buried oxide (BOX) at 12 locations. Handle layer resonators are partially stacked underneath device layer resonators.

First, the SOI wafer was processed.  $1.5 \mu\text{m}$   $\text{SiO}_2$  were deposited by PECVD on top of the device layer (figure 7, 1(a)), which was then patterned using photolithography and reactive ion etching (RIE) (figure 7, 1(b) + (c)). Afterwards, the obtained  $\text{SiO}_2$  hard mask was protected with photoresist, the wafer flipped and photolithography performed on the handle layer (figure 7, 1(d)). Next, the thermal  $\text{SiO}_2$  was selectively removed with RIE and the masses and springs in the handle layer were formed with deep reactive ion etching (DRIE), with the photoresist still protecting the thermal oxide (figure 7, 1(e)). Lastly, the SOI wafer was cleaned with a mixture of  $\text{H}_2\text{SO}_4:\text{H}_2\text{O}_2$  (3:1) (figure 7, 1(f)). Secondly, a DSP support wafer was patterned with cavities and also cleaned (figure 7, 2(a)–(c)). Thirdly, the SOI and support wafer were aligned and bonded at  $250^\circ\text{C}$  in a hydrophilic direct bonding process [22] (figure 7, 3(a)). Afterwards, the wafer stack was annealed at  $1000^\circ\text{C}$  for 5 min in argon ambient to decrease intrinsic stress and was then diced. The single dies were attached with white wax on a carrier wafer and masses and springs in the device layer were defined with DRIE (figure 7, 3(b)). Finally, the resonators in the device layer were released with vapor hydrofluoric acid (HF) (figure 7, 3(c)). Designed DRIE aspect ratios for the springs were 500:27 in the handle layer and 40:1.3 in the device layer.

According to the design rule (1), the individual resonators should all have matching eigenfrequencies. However, spring thicknesses and thus spring stiffnesses are heavily influenced by the fabrication process. Springs of one layer are processed together and similarly influenced as long as their designed spring thickness is the same. Since aspect ratios of the springs in the respective layers differ widely, two different DRIE recipes have to be used. Thus the eigenfrequencies of resonators of one layer have to be matched to the eigenfrequencies in the other one. Uncoupled resonators were used as test structures to find parameters for an optimal match (see supplementary data, section 2).

#### 3.2. Characterization

The final device was optically characterized with a laser Doppler vibrometer (LDV) to verify the design and fabrication process (figure 8). Even though the device has a capacitive readout at  $m_{10}$ , optical characterization is preferable in lab environment as it allows to track the movement of individual resonators and to assess the purely mechanical

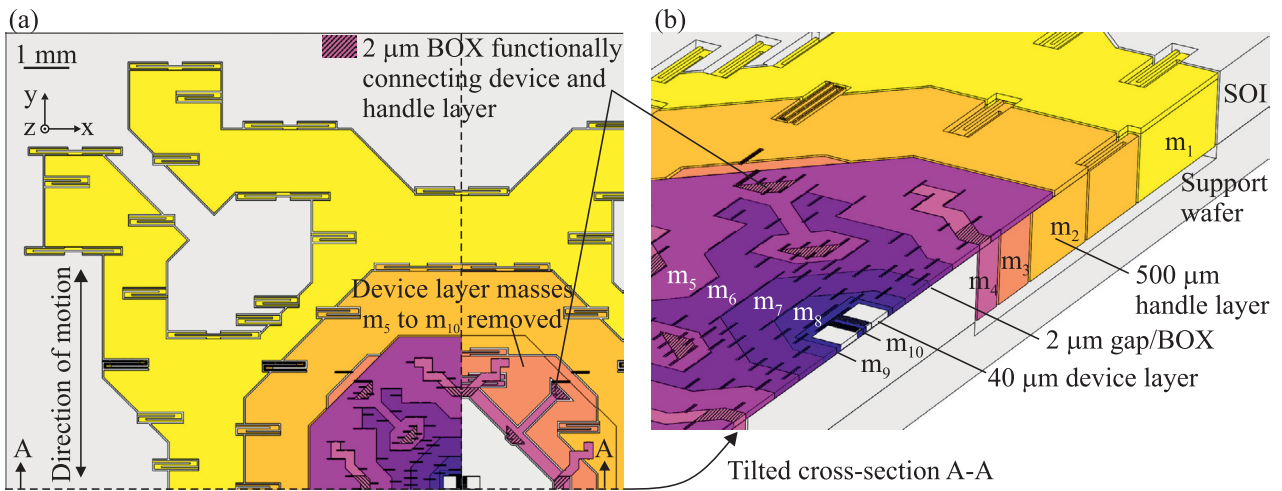


**Figure 6.** (a) Top view of a corner of the two-fold symmetric design (CAD drawing). On the right-hand side resonators in the device layer are removed such that resonators underneath can be seen. (b) Tilted cross-section view of the design (A–A). Device layer and handle layer are functionally connected at  $m_4$  through small unreleased islands.

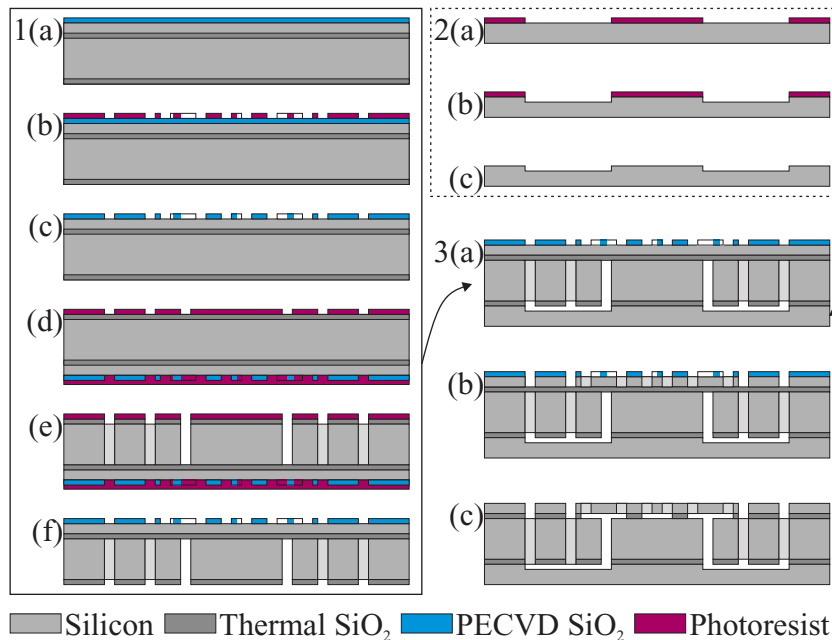


**Figure 7.** 1. Processing of SOI wafer: 1(a) PECVD of  $\text{SiO}_2$  on top of device layer. 1(b) + (c) Patterning of PECVD  $\text{SiO}_2$ . 1(d) Protection of  $\text{SiO}_2$  hard mask and photolithography of handle layer. 1(e) RIE followed successively by DRIE to pattern masses and springs in handle layer. 1(f) Wafer cleaning. 2. Processing of support wafer: 2(a) Photolithography of double-side-polished wafer. 2(b) DRIE etching of cavities. 2(c) Wafer cleaning. 3. Processing of SOI and DSP wafer: 3(a) Hydrophilic direct wafer bonding, annealing at  $1000\text{ }^\circ\text{C}$  and dicing. 3(b) DRIE of device layer masses and springs. 3(c) Vapor HF release.

transfer functions. The device was mounted vertically on a piezoelectric actuator which was fixed at a flat angle ( $15^\circ$  was chosen). Characterization was performed in a vacuum chamber with a glass cover plate. The laser of the LDV was focused on the resonator of interest where etched surfaces (e.g. etch-holes, side walls) reflected enough light.

The sample was actuated with a chirp signal and the motion of the resonator of interest as well as the piezoelectric actuator were measured. The mechanical transfer functions were obtained by normalizing the spectral displacement of the resonator of interest with the spectral displacement of

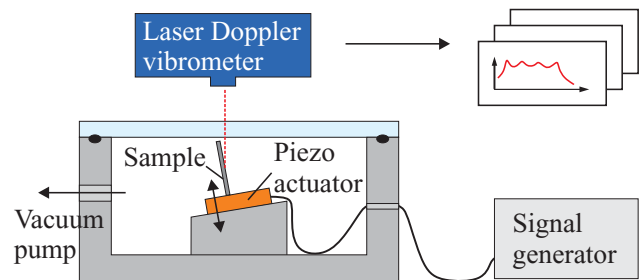


**Figure 8.** Samples were optically characterized with a laser Doppler vibrometer to verify design and fabrication.

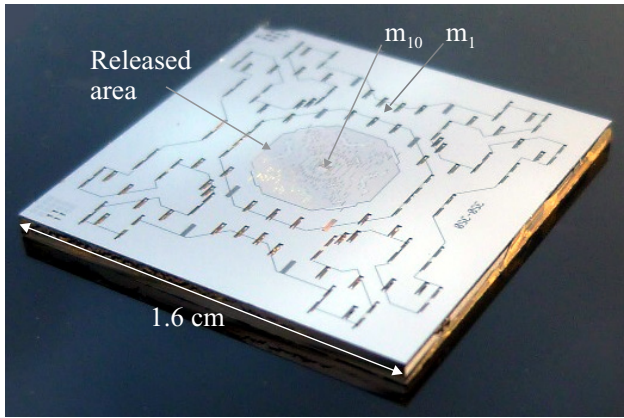


**Figure 9.** Photo of the multiscale device with indicated masses  $m_1$ ,  $m_{10}$  and released area. Dies are  $1.6 \times 1.6$  cm large.

the piezoelectric actuator. For the transient measurements, a sinusoidal signal of given frequency was used and actuation and measurement signal were synchronized by using the triggering function of the LDV. Measurements were normalized by the input amplitude of the piezoelectric actuator. All measurements were taken with the velocity decoder. To obtain the displacement in the transient measurements, the results were integrated and random low frequency noise was removed by subtracting the moving average over one oscillation period.

The mode shapes were experimentally obtained from the transfer functions and phase plots of all individual resonators and then compared to the ones of an FEA simulation. The simulation included fabrication deviations of spring thicknesses in the device and handle layer taken from SEM images (see supplementary data, section 3) eigenvectors with motion amplitudes obtained from the experiments and FEA simulation were normalized to length one.

The resonator motions of the device are unidirectional by design in the bandwidth of interest. Thus a 1D lumped element model can be assumed. Differential equations of a multi-DOF 1D lumped element model can be found in e.g. [23]. For comparison,  $f_0$  of the model was matched to  $f_0$  of the experimental results. The parameters of the damping matrix of the model were fitted similar to [10], which accounts for the squeeze film damping of the capacitive readout fingers at  $m_{10}$ . Additionally, spring thicknesses in the device and handle layer measured in SEM images were taken into account.

## 4. Results

### 4.1. Fabrication

A photo of the fabricated multiscale device is given in figure 9. Dies are  $1.6 \times 1.6$  cm large, with  $\frac{1}{13}$  of the device layer area ( $20 \text{ mm}^2$ ) released. A closer view of one quarter of the released area is shown in an SEM picture (figure 10(a)). All resonators with etch-holes belong to the device layer and are suspended in the final vapor HF release ( $m_5$ – $m_{10}$ , colored for better visibility). A tilted SEM picture of the backside of the same device with removed support wafer is also presented

(figure 10(b)). The handle layer resonators underneath the device layer resonators are fully visible from this side.

A successful release of all device layer resonators was verified with white light interferometry (WLI) (figure 11). The device layer masses are flat, but 350 nm out-of-plane deflected compared to the handle layer. This is attributed to stress induced strain in the SOI wafer. Out-of-plane deformations are less than  $1 \mu\text{m}$  over a device size of  $1.6 \times 1.6$  cm.

### 4.2. Characterization

The fabricated devices were optically characterized and results were compared to a lumped element model and FEA simulations. The steady-state response, including eigenfrequencies and mode shapes, and transient response as well as influence of pressure were investigated.

**4.2.1. Steady-state response.** The transfer function of mass  $m_{10}$  was measured at 1.6 mbar (figure 12). The amplitude of  $m_{10}$  ( $Y_{10}$ ) is normalized by the input amplitude ( $Y_0$ ). Ten resonance peaks corresponding to a lumped element model with ten coupled masses are visible. Average amplification over a bandwidth of 10.68 kHz (4.37–15.05 kHz) is 295 (49.4 dB), with a minimum amplification of 63 (36.0 dB). The lumped element model based on the as fabricated geometry (spring stiffnesses) fits the experimental results. The last valley and peak are slightly lowered, and the bandwidth is wider compared to a system with perfect frequency match of the resonators in both layers (compare to figure 4, springs are 6% stiffer in the device than in the handle layer).

The first ten resonant frequencies of the device were obtained from the measured transfer function of  $m_{10}$  and are given in table 1. They are compared to the resonant frequencies of the (damped) lumped element model and natural frequencies from the (undamped) FEA simulation. The lumped element model deviates from the measurement maximally by 1.8% and the FEA by 2.8%.

Further, the mode shapes of the device are compared to FEA simulation (figure 13). Only the first three and the last mode are shown for brevity. Experimental and simulation results show zero nodes for the 1st mode and one, two respectively nine nodes for the 2nd, 3rd and 10th mode. The root-mean-square deviation is for the 1st mode 17%, for the 2nd 7%, the 3rd 7% and the 10th 22%.

**4.2.2. Transient response.** Off-resonant responses of resonators  $m_5$ – $m_{10}$  were measured between the first two eigenfrequencies at 4.9 kHz (figure 12). They are normalized by the amplitude of the piezo actuator  $Y_0$  (figure 14(a)). Motion amplitudes increase from mass to mass, with the last mass displaying the highest amplitudes ( $y_{10}$ ). The responses show first some evidence of beat modulation and turn then into a steady oscillation with nearly constant amplitude, which corresponds to the off-resonant response of driven damped harmonic oscillators [24].

A closeup of the initial response reveals the shoaling amplification (figure 14(b)). The mass directly connected to

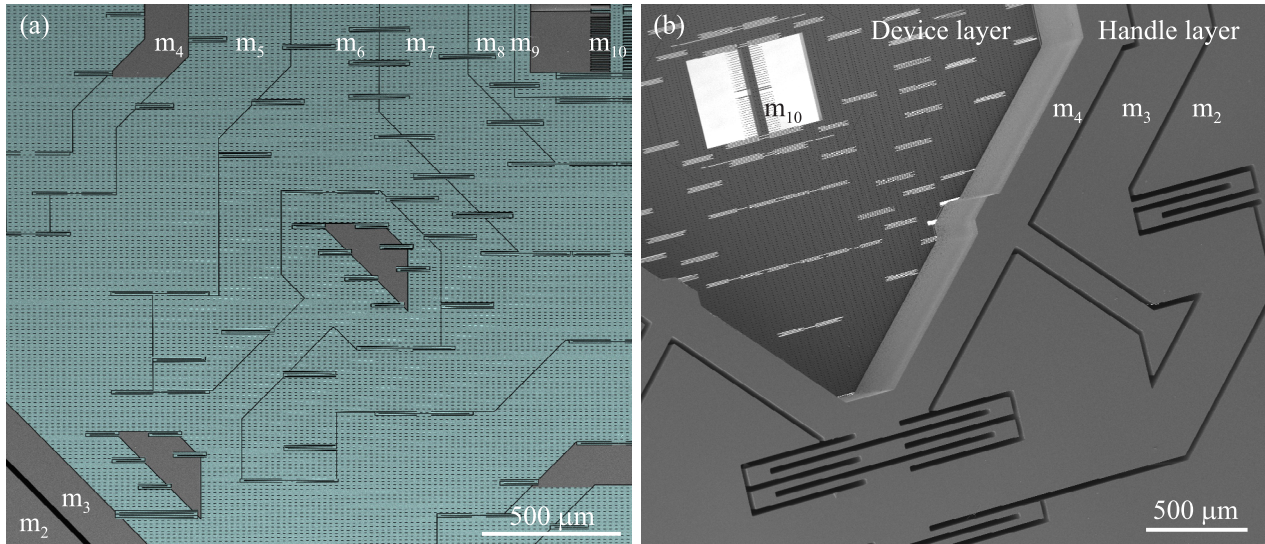


**Figure 10.** (a) Top view of a quarter of the device. Released area is colored for better visibility. (b) Tilted SEM picture of backside of device with removed support wafer.

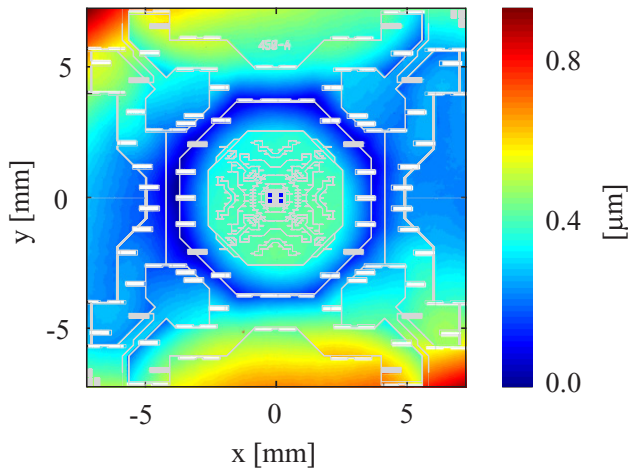


**Figure 11.** White light interferometer picture of a device. Device layer resonators are 350 nm out-of-plane deflected compared to handle layer resonators.

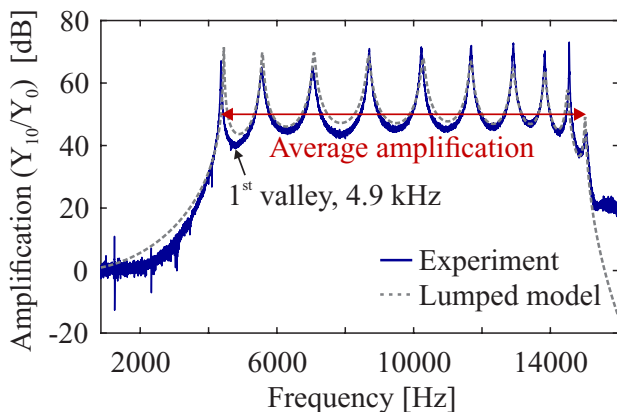


**Figure 12.** Mechanical transfer function of  $m_{10}$ . An average amplification of 295 (49.4 dB) is achieved from first to last resonance frequency (4.45–15.05 kHz). The ten resonance peaks of the device correspond well with the lumped element model.

**Table 1.** Comparison of resonances obtained with measurement, lumped element model and FEA simulation.

Mode	Shape <sup>a</sup>	Experiment	Lumped model	FEA
$\nu_1$	IP	4.37	4.45	4.33
$\nu_2$	IP	5.55	5.58	5.44
$\nu_3$	IP	7.05	7.10	6.87
$\nu_4$	IP	8.71	8.70	8.48
$\nu_5$	IP	10.23	10.29	10.01
$\nu_6$	IP	11.69	11.68	11.40
$\nu_7$	IP	12.92	12.93	12.65
$\nu_8$	IP	13.84	13.86	13.55
$\nu_9$	IP	14.55	14.52	14.23
$\nu_{10}$	IP	15.05	15.05	14.63
$\nu_{11}$	OP	—	—	16.00

<sup>a</sup> In-plane (IP) or out-of-plane (OP).

the substrate is excited first. The excitation wave then travels from mass to mass and its amplitude is steadily increased until it reaches the last mass  $m_{10}$ . The input excitation amplitude is thus amplified.

Figure 15 shows how long the response time is to reach average amplification at the last mass. It takes less than 1 ms between 5–14 kHz. Outside this bandwidth average amplification is never reached. Lumped element model values are very similar to the experimentally measured response time.

**4.2.3. Influence of pressure.** The transfer function for  $m_{10}$  for different pressures is shown in figure 16. While the Q-factors of the resonance peaks decrease for higher pressure, the off-resonant amplification remains. Especially the last resonances are heavily influenced by higher pressure, at 16 mbar the last resonance has fully vanished. Average amplification and bandwidth for different pressures are: 5.4 mbar: 294×, 10.68 kHz; 16 mbar: 315×, 10.18 kHz; 46 mbar: 230×, 10.15 kHz.



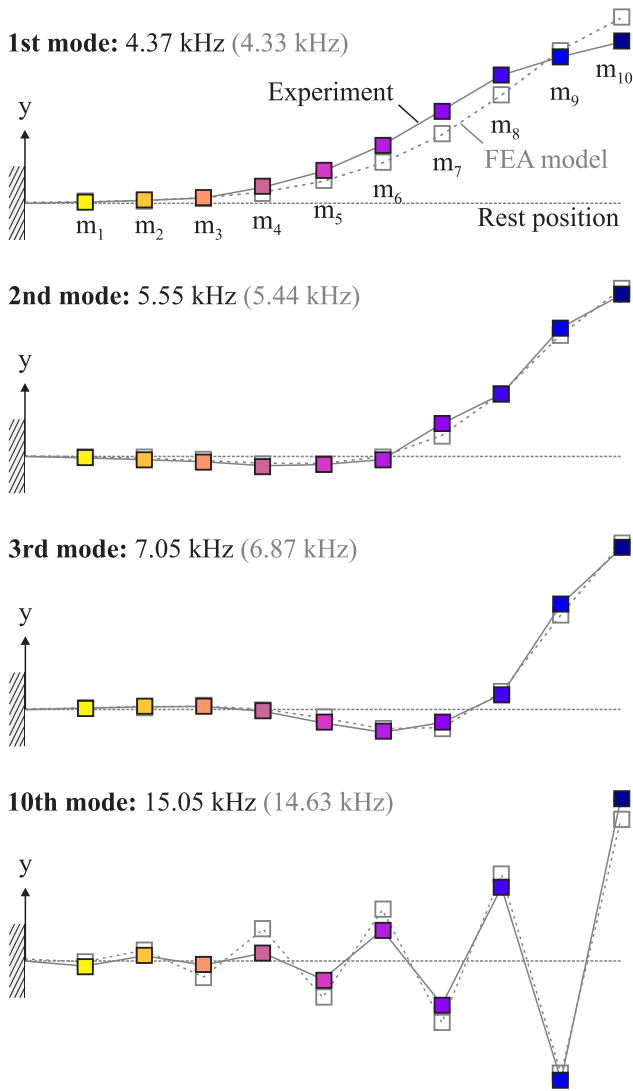


**Figure 13.** Measured mode shapes compared to FEA simulation. For brevity, only the first three and the last mode are shown. Number of nodes are equal for experimental data and FEA simulation.

### 5. Discussion

In this chapter, design and device fabrication are discussed, agreement of measurement and simulation results are assessed and device performance is evaluated.

#### 5.1. Design and fabrication

There are two main challenges for the two-level multiscale device design and fabrication. First, intrinsic stress and resulting warping must be low to assure full functionality of the device. Secondly, frequency matching of the resonators in the two levels has to be achieved for an undistorted amplification band.

Warping of released structures in SOI wafers is a well-known issue [21]. Especially large released areas, as is the case in the presented device, suffer. The further away a structure is from the anchor to the underlying handle layer, the larger the effect of warping becomes. The last mass is thus

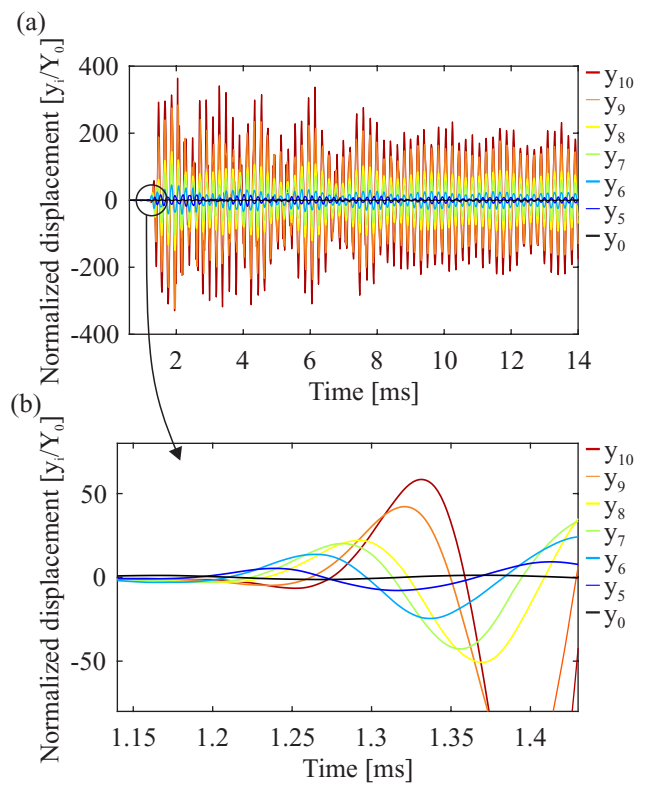


**Figure 14.** (a) Transient response of masses  $m_5$ – $m_{10}$  for a sine excitation of 4.9 kHz at 1.6 mbar. The responses are normalized to the excitation amplitude  $Y_0$ . (b) A close-up of the circled area shows the shoaling amplification of the incoming excitation wave.

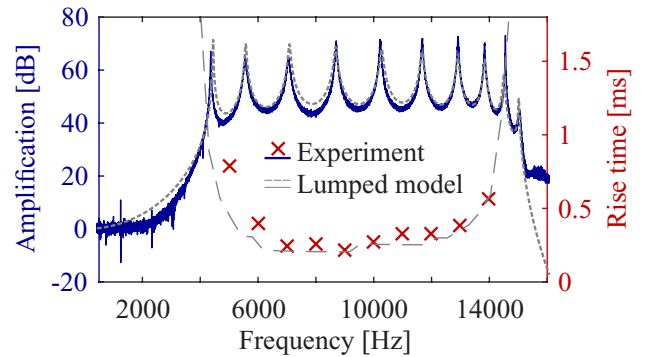


**Figure 15.** Required time for  $m_{10}$  to reach average amplification (295, 49.4 dB) over the frequency range of interest. Average amplification is reached in less than 1 ms between 5–14 kHz.

the most affected in our case. For a working device, less than  $2 \mu\text{m}$  downwards out-of-plane deflection of  $m_{10}$  (in negative  $z$ -direction in figure 11) and less than  $1.1^\circ$  in-plane rotation due to warping must be achieved to assure undisturbed oscillation. Low intrinsic stress, which lead to only 350 nm upwards out-of-plane deflection of the last resonator compared to the handle layer / support wafer underneath, was achieved by choosing materials and fabrication processes carefully (see section 3.1).

Even though DRIE is a fairly repeatable process step, achieved spring thicknesses may vary from run to run and further depend on chip location. The presented device shows 6% stiffer springs in the device layer than in the handle

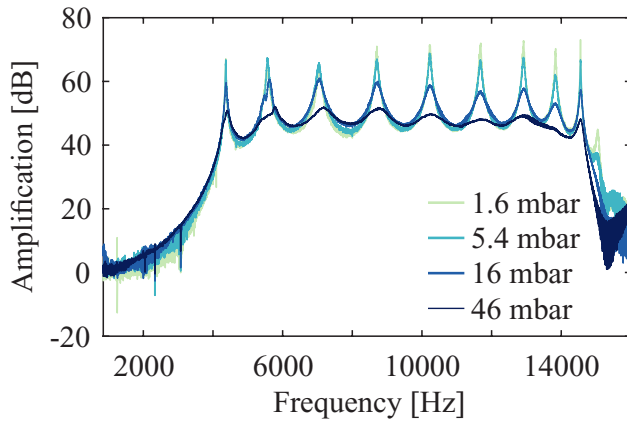


Figure 16. Transfer function of  $m_{10}$  at different pressures.

Table 2. Device specifications at 1.6 mbar.

Parameter	Value
Die size	$1.6 \times 1.6$ cm
$m_1$	$9.1 \times 10^{-5}$ kg
$m_{10}$	$3.5 \times 10^{-9}$ kg
Min. amplification	63 (36.0 dB)
Average amplification	295 (49.4 dB)
Bandwidth	10.7 kHz (4.37–15.05 kHz)
Response time	<1 ms between 5–14 kHz

layer, which still resulted in a regular transfer function with clearly defined bandwidth (figure 12 compared to figure 4). Spring stiffnesses of thicker springs are less heavily affected by process variations. Thus, thicker springs could improve the frequency matching of the two layers. However, thicker springs are also less selective, which may introduce gimbal, rotational or out-of-plane modes within the first ten eigenmodes. Another option to increase the frequency matching would be to improve the repeatability of the DRIE process.

### 5.2. Comparison of measurements and simulations

Resonance frequencies of measurements and simulations agree within 2.8% deviation (table 1) and measured mode shapes verify that the ten resonance modes are in-plane in the sensitive direction and correspond to the eigenmodes of a classical coupled mass-spring system with ten DOF (figure 13). There are no detectable out-of-plane, rotational or gimbal mode shapes within the amplification bandwidth. While the number of nodes and general shapes correlate between the measurement and FEA simulation, there is some disagreement for the mass motion amplitudes. The root-mean-square deviation is for the shown modes highest at the 10th mode (22%).

Finally, damping was included in the lumped element model, but the chosen damping matrix does not fully represent the complex damping mechanisms in the device, which results in deviating resonance amplitudes (figure 12).

### 5.3. Device performance

The main specifications of the fabricated device are summarized in table 2 and essential characteristics including amplitude amplification, bandwidth and response time are discussed in this section.

The measured minimum amplification is 58% lower than targeted due to the mentioned frequency mismatch of the resonators in the handle and device layer. The low amplification is limited to a very narrow frequency range and should not strongly influence the detection of broadband vibration bursts. The average amplification is influenced by damping, but off-resonant amplification is unaffected in the measured pressure range from 1.6–46 mbar (figure 16). Depending on application targets, the resonance peaks can be flattened out with a low vacuum packaging, thus the reliability of the device is increased at the cost of weaker detection resolution.

The bandwidth is shifted by 1.7 kHz to lower frequencies compared to the target specifications due to softer springs, but it is still in the frequency range of low acoustic emissions (measured  $f_0 = 10.8$  kHz, designed  $f_0 = 12.5$  kHz).

The measured response time of under 1 ms is crucial for the application of the mechanical amplifier. Vibration bursts can consist of only a few oscillations and would otherwise not be detected. Amplifiers relying on resonance (e.g. single high-Q resonators) require several oscillations to build up a high amplitude and thus are less suitable to detect burst signals.

## 6. Conclusion

A two-level fabrication process for a multiscale device has been presented. Ten resonators, ranging from  $3.5 \times 10^{-9}$  to  $9.1 \times 10^{-5}$  kg, could be successfully connected in series to achieve an average amplitude amplification of 295 over a bandwidth of 10.7 kHz (4.4–15.1 kHz). The average amplification is reached in less than 1 ms from 5–14 kHz. Resonators were stacked on top of each other in the two layers to decrease device size. This fabrication process may be of interest to other multiscale devices. Future work will include packaging at a specific pressure and electrical characterization of the device. Even more resonators might be added to achieve a higher amplification. Also, a pull-in readout could be integrated in the device [25], which would allow for ultra-low power detection of short vibration bursts.

## Acknowledgments

This project was scientifically evaluated by the Swiss National Science Foundation (SNSF), financed by the Swiss Confederation and funded by Nano-Tera.ch. The authors would like to thank Yunjia Li and Stéphane Kühne for fruitful discussions and advice in process development. The ETH FIRST-CLA and BRNC cleanroom staff (especially Donat Scheiwiller and Ute Drechsler) are acknowledged for their invaluable support with fabrication.

## ORCID iDs

Michelle Müller  <https://orcid.org/0000-0003-0825-0285>

## References

- [1] Girard L, Gruber S, Weber S and Beutel J 2013 *Geophys. Res. Lett.* **40** 1748–53
- [2] Zeimpekis I, Sari I and Kraft M 2012 *J. Microelectromech. Syst.* **21** 1032–42
- [3] Khan S and Ananthasuresh G K 2014 *J. Microelectromech. Syst.* **23** 871–87
- [4] Li X, Lin R and Leow K W 2000 *J. Micromech. Microeng.* **10** 534–9
- [5] Wei M, De Pasquale G, Wang J and Soma A 2009 Capacitively-transduced mechanically-coupled bandpass filter in electroplated nickel for harvesting energy from ambient vibrations *Proc. of PowerMEMS* pp 213–6
- [6] Zhou W, Penamalli G R and Zuo L 2012 *Smart Mater. Struct.* **21** 015014
- [7] Aladwani A, Aldraihem O and Baz A 2014 *Mech. Adv. Mater. Struct.* **21** 566–78
- [8] Vullers R, Elfrink R, Matova S and Wang Z 2012 Large power amplification of MEMS harvester by a secondary spring and mass assembly *Proc. PowerMEMS* pp 211–4
- [9] Maiwald V, Müller M, Ritz C, Roman C and Hierold C 2017 Shoaling vibration amplifier with flattened transfer function and suppressed spurious modes *IEEE 30th Int. Conf. on Micro Electro Mechanical Systems* pp 1154–7
- [10] Maiwald V, Müller M, Ritz C, Hierold C and Roman C 2017 *J. Microelectromech. Syst.* **26** 1345–55
- [11] Müller M, Maiwald V, Käch M, Hierold C and Roman C 2015 A passive micromechanical broadband amplifier for acoustic emission sensing *TRANSDUCERS 2015—18th Int. Conf. on Solid-State Sensors, Actuators and Microsystems* pp 1129–32
- [12] Abdolvand R, Amini B and Ayazi F 2007 *J. Microelectromech. Syst.* **16** 1036–43
- [13] Xie J, Song M and Yuan W 2013 A high sensitivity micromachined accelerometer with an enhanced inertial mass SOI MEMS process *8th Annual IEEE Int. Conf. on Nano/Micro Engineered and Molecular Systems* vol 1 (IEEE) pp 336–9
- [14] Classen J, Reinmuth J, Kalberer A, Scheurle A, Gunther S, Kiesel S, Schellin B, Brauer J and Eicher L 2017 Advanced surface micromachining process—a first step towards 3D MEMS *IEEE 30th Int. Conf. on Micro Electro Mechanical Systems* pp 314–8
- [15] Comtois J, Michalicek M and Barron C 1997 Characterization of electrothermal actuators and arrays fabricated in a four-level, planarized surface-micromachined polycrystalline silicon process *Proc. of Int. Solid State Sensors and Actuators Conf.* pp 769–72
- [16] Bannon F D, Clark J R and Nguyen C C 2000 *IEEE J. Solid-State Circuits* **35** 512–26
- [17] Wang K and Nguyen C T 1999 *J. Microelectromech. Syst.* **8** 534–57
- [18] Elka A and Bucher I 2008 *J. Micromech. Microeng.* **18** 125018
- [19] Weber S, Gruber S, Girard L and Beutel J 2012 Design of a measurement assembly to study *in situ* rock damage driven by freezing *Proc. of the 10th Int. Conf. on Permafrost* pp 437–42
- [20] Baran I, Lyasota I and Skrok K 2016 Acoustic emission testing of underground pipelines of crude oil of fuel storage depots *J. Acoust. Emiss.* vol **33** pp 125–36
- [21] Tilli M, Motoooka T, Airaksinen V M, Franssila S, Paulasto-Krockel M and Lindroos V 2015 *Handbook of Silicon Based MEMS Materials and Technologies (Micro and Nano Technologies)* (Amsterdam: Elsevier)
- [22] Kühne S and Hierold C 2011 *J. Micromech. Microeng.* **21** 085032
- [23] Meirovitch L 1975 *Elements of Vibration Analysis* Int. Student edn (New York: McGraw-Hill)
- [24] Garrett S L 2017 *The Simple Harmonic Oscillator* (Berlin: Springer) pp 69–152
- [25] Maiwald V, Chen Y, Müller M, Flader I, Roman C, Heinz D, Shin D, Kenny T and Hierold C 2017 Transfer function tuning of a broadband shoaling mechanical amplifier near the electrostatic instability *TRANSDUCERS 2017—19th Int. Conf. on Solid-State Sensors, Actuators and Microsystems* pp 802–5